Pattern selection for convective flow in a liquid bridge subjected to remote thermal action.

Y. Gaponenko,[1] T. Yano,[2] K. Nishino,[3] S.Matsumoto,[4] and V. Shevtsova[5,6]
[1)]*Microgravity Research Center, CP-165/62, Université libre de Bruxelles (ULB), 50, Ave. F.D. Roosevelt, B-1050 Brussels, Belgium*
[2)]*Department of Mechanical Engineering, Kanagawa University, 3-27-1 Rokkakubashi, Kanagawa-ku, Yokohama, Kanagawa 221-8686, Japan*
[3)]*Department of Mechanical Engineering, Yokohama National University, 79-5 Tokiwadai, Hodogaya-ku, Yokohama, Kanagawa 240-8501, Japan*
[4)]*Japan Aerospace Exploration Agency, 2-1-1 Sengen, Tsukuba, Ibaraki 305-8505, Japan*
[5)]*Mechanical and Manufacturing Department, Mondragon University, Loramendi 4, Apdo. 23, 20500 Mondragon, Spain*
[6)]*Basque Foundation for Science, Bilbao, Spain*

(*Electronic mail: x.vshevtsova@mondragon.edu)

(Dated: 24 October 2022)

The stability of thermocapillary/buoyant flows is affected by a remote thermal source. We present a nonlinear two-phase computational study of convection in a liquid bridge that develops under the action of Marangoni and buoyancy forces, as well as under the influence of distant thermal disturbances. The gas phase (air) occupies a typical annular container holding a liquid bridge (n-decane, Pr=14), and the disturbances are locally imposed in the form of hot/cold spots on the outer wall of the container. The hydrothermal wave instability and pattern selection have been explored for two temperature differences ΔT by varying the intensity of thermal source H_f over a wide range. Not far from the critical point, in all the cases, the instability emerges in the form of a standing wave, but the azimuthal wavenumber depends on whether the external perturbation is caused by cooling (m=2) or by heating (m=1). Further into supercritical area, 45% above the threshold, in the region with thermal perturbations $-200 < H_f < 50$, the flow pattern comprises, but is not limited to, a hydrothermal traveling wave with the azimuthal wavenumber m=2. For hotter perturbations, the instability develops either in the form of traveling or standing waves, depending on H_f, with the prevailing mode m=1, but with a strong presence of other modes.

I. INTRODUCTION

Multiphase systems including gas-liquid interfaces in contact with solids appear in various industrial applications. Temperature gradients along the interface cause variations of surface tension resulting in tangential stresses which can drive bulk flow motion. This effect of thermocapillary flow is very important in many scientific studies and technological implementations such as crystal growth[1,2], welding[3], combustion[4], thermal energy storage[5,6] and liquids handling in microsystems[7].

Interest in the study of thermocapillary convection in a liquid bridge was initially associated with the process of crystal growth, when the liquid bridge began to be considered in experimental configurations of half-zone models[8] in order to simplify the problem. In this model, the liquid bridge is a droplet of fluid suspended between two concentric disks maintained at different temperatures T_{hot} and T_{cold}. At a small temperature difference, $\Delta T = T_{hot} - T_{cold}$, the flow is a steady axisymmetric toroidal vortex. When the temperature difference ΔT exceeds the critical value ΔT_{cr}, hydrothermal instability sets in as a result of a Hopf bifurcation and causes an oscillatory flow as the first or secondary instability depending on Prandtl number[9–12]. The stability of the flow in a thermocapillary liquid bridge (LB) is a complex problem, and the emergence and evolution of hydrothermal waves were initially studied in a one-phase approximation in different geometries and aspect ratios [13–19].

Experimental evidence for the important role of heat transfer through the liquid–gas interface in the stability of the thermocapillary flow in LB has been reported since the 1980s. A series of experiments were carried out in Earth[20–25] and orbital[24,26,27] laboratories monitoring the ambient conditions around a liquid bridge, which indicated that heat exchange between the liquid and the ambient gas is an important factor that affects the mechanisms of instability. Subsequent numerical studies employed single-phase 3D numerical simulations using Newton's law to take into account a heat transfer through the interface. The different temperature conditions in the gas phase were considered[28–31]: the constant temperature equal either to T_{cold} or T_{hot}, or the linear distribution.

The flow in the surrounding gas is driven by the liquid shear. Even though the gas/liquid viscosity ratio is low, the gas motion changes the temperature distribution near the interface. Thus, consideration of the two-phase problem brings numerical predictions closer to experimental observations[32,33]. Particular attention to the role of viscous shear was given in the numerical analysis by Shevtsova et al.[34] considering axisymmetric flows in LB at relatively high velocities of the ambient gas flow. The moving gas with various temperatures and velocities provides the possibility to influence non-linear dynamics of the system and control the onset of hydrothermal waves. It motivated the preparation of the forthcoming orbital experiment JEREMI[35,36] and activated two-phase simulations with moving gas[37–39].

Still, comparison of two-phase simulation for intricate ther-

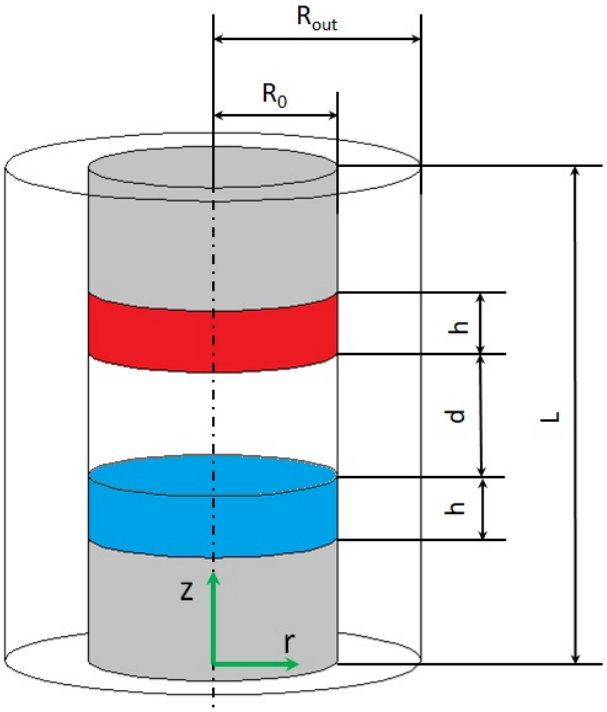

FIG. 1. Sketch of the geometry.

mocapillary flow with experimental observations, as a rule, provides qualitative agreement, and quantitative agreement requires the adjustment of the parameters. For instance, recent very accurate but complicated experiments in a liquid bridge with a coaxial gas flow required a shift of ΔT by 4 K to get an excellent agreement of nonlinear dynamics comparing with simulations[37]. Surely, the numerical model is ideal and does not take into account imperfections of experimental arrangement, for example, small non-flatness of supporting disks[33]. A two-dimensional axisymmetric motion equivalent to a Marangoni convection at $\Delta T = 0.2\,K$ was observed in a liquid bridge experiment without obvious driving force[40]. The great interest presents the analysis of thermal disturbances, which can be created by a working camera, laser, etc. In this context, the present study is aimed at understanding the influence of a remote thermal impact on the dynamics of hydrothermal waves in the liquid bridge surrounded by gas.

The paper is organized as follows. The two-phase mathematical model with appropriate boundary conditions is formulated in Sec. II. Section III includes detailed analysis of hydrothermal instability for two values of ΔT at different distance from the critical point. For each ΔT, we examine the evolution and properties of hydrothermal waves, while intensity of the thermal disturbances varies over a wide range from cold to hot. The section is ended by a short overview of the results. Concluding remarks are presented in Sec. IV.

II. PROBLEM FORMULATION

A. Geometry

We study the two-phase thermocapillary flow in a liquid bridge in the geometry similar to that employed in [34,36,37], where focus was placed on non-linear dynamics and flow patterns. The sketch of the three-dimensional model is shown in Fig. 1. The system consists of two co-axial cylinders. The inner cylinder is surrounded by a long tube. The space between the inner cylinder and the external tube is filled initially motionless gas. The inner cylinder consist of two solid rods of the radius R_0=3.0 mm and a liquid bridge between them of the height d =3.0 mm, which is kept in its position by the surface tension force. The radius of the external tube is R_{out}=5 mm. Each rod has the length 4.5 mm, while the thickness of the heating/cooling parts of the rods is h=1.5 mm. The total length of the system is L=12 mm. The length of the inert part of the rod below (above) the cold (hot) disk is h_{in}=0.5(L-d-2h)=3mm.

B. Governing equations

Both the liquid and the gas are considered as Newtonian fluids with the linear temperature-dependent density ρ and the surface tension σ. Viscosity μ is taken at mean temperature, $T_0 = 298\,K$, and considered as a constant in this study because the variation of ΔT is not very large. The working fluids are n-decane and air, the physical properties of which are given in Table I.

The purpose of the study is to investigate the effect of thermal perturbations on the outer wall on flow dynamics. The problem is treated in the framework of the Boussinesq approximation such that density variations are only taken into account in the buoyancy body-force term. The three-dimensional dynamics of the system in the geometry of Fig. 1 is described by the momentum, heat transfer and continuity equations for incompressible Newtonian fluids in liquid and gas phases as:

$$\partial_t \vec{V} + (\vec{V}\cdot\nabla)\vec{V} = -\frac{1}{\rho_0}\nabla p + \nu\,\nabla^2\vec{V} - \vec{g}\beta_T(T-T_0) + \vec{g}, \quad (1)$$

$$\partial_t T + \vec{V}\cdot\nabla T = \chi\nabla^2 T, \quad (2)$$

$$\nabla\cdot\vec{V} = 0, \quad (3)$$

where $\vec{V}$ and p denote the velocity and pressure fields, T is the temperature, $\nu = \mu/\rho_0$ is the kinematic viscosity, χ is the thermal diffusivity and $\vec{g}$ is the gravity vector. Since the equations for liquid and gas are identical, the superscripts "l" (liquid) and "g" (gas) are dropped in the formulation.

C. The initial and boundary conditions

In the considered case of n-decane the static Bond number is relatively small, $Bo_{st} = \rho g d^2/\sigma$=2.7, and the effect of

TABLE I. Physical properties of n-decane and nitrogen at 298 K: the dynamic viscosity μ, the thermal diffusivity χ, the thermal conductivity k, the density ρ, the thermal expansion $\beta_T = -(1/\rho_0)d\rho/dT$, the Prandtl number $Pr = \nu/\chi$. The surface tension is σ=23.83 (293 K) mN/m. The thermal characteristic time of liquid is $\tau_{ch} = d^2/\chi \approx 107\,s$.

fluid	μ (Pa· s)	χ (m^2/s)	k (W/m K)	ρ (kg/m^3)	$\beta_T/10^{-3}$ (1/K)	Pr	$\sigma_T = -d\sigma/dT$ (N/mK)
n-decane	$84.70\cdot10^{-5}$	$8.45\cdot10^{-8}$	0.135	726.27	1.06	13.8	$1.18\cdot10^{-4}$
air	$1.79\cdot10^{-5}$	$2.24\cdot10^{-5}$	0.025	1.225	3.17	0.71	

static deformation will not be considered. According to the perturbation expansion shown by Montanero et al.[41] for small Bond numbers, for short liquid bridges there is a partial mutual cancellation of a linear and a sinusoidal perturbation of opposite signs, both proportional to the static Bond number. Due to this cancellation, the maximum free surface deformation of first order in the Bond number is approximately given by $|R-R_0|_{max}/R_0 \approx 0.0084\,\Gamma\,Bo_{st}$. For the unit aspect ratio Γ it provides static deformation of 0.0068 mm for a liquid bridge of R_0=3 mm and can be neglected.

1) The boundary conditions on the free surface $r = R_0$ between the liquid and gas are:

(a) the balance of viscous and thermocapillary forces is

$$\left[P_l - P_g\right] n_i - \left(S^l_{ik} n_k - S^g_{ik}\, n_k\right) = \frac{\sigma}{\mathscr{R}} n_i - \frac{\partial \sigma}{\partial x_i} \tag{4}$$

where $S_{ik} = S = \mu(\partial V_i/\partial x_k + \partial V_k/\partial x_i)$ is the viscous stress tensor, $\mathscr{R}$ is the curvature, and the unit normal vector $\vec{n}$ is directed out of the liquid. Since the interface shape is fixed, the normal projection of Eq. (4) is not considered. The tangential projections of Eq. (4) define the driving thermocapillary force in axial and azimuthal directions, j=1,2

$$\tau^j \cdot \mathbf{S}^l \cdot \mathbf{n} - \tau^j \cdot \mathbf{S}^g \cdot \mathbf{n} = -\tau^j \cdot \nabla\sigma \tag{5}$$

(b) The tangential velocities of the liquid and gas are equal.

$$\vec{V}^l_\tau = \vec{V}^g_\tau; \tag{6}$$

(c) The kinematic condition at the non-deformable interface provides $V_n = 0$.

(d) The heat fluxes and temperatures of the liquid and gas are equal; here k is the thermal conductivity

$$k^l\ \partial_n T^l = k^g\ \partial_n T^g, \qquad T^l = T^g. \tag{7}$$

2) The lateral surfaces of the rods, which are in contact with gas, are thermally insulated and no-slip conditions are imposed:

$$\begin{aligned} &\text{when} \quad 0 \le z \le h_{in}; \quad (L-h_{in}) \le z \le L; \\ &\partial_n T = 0 \qquad \text{and} \qquad \vec{V}^g(r=R_0) = 0 \end{aligned} \tag{8}$$

3) The small parts of the rods (thickness h) at the bottom and top, respectively, are kept at constant temperatures

$$T = T_0 - \Delta T/2 \quad \text{and} \quad T = T_0 + \Delta T/2 \tag{9}$$

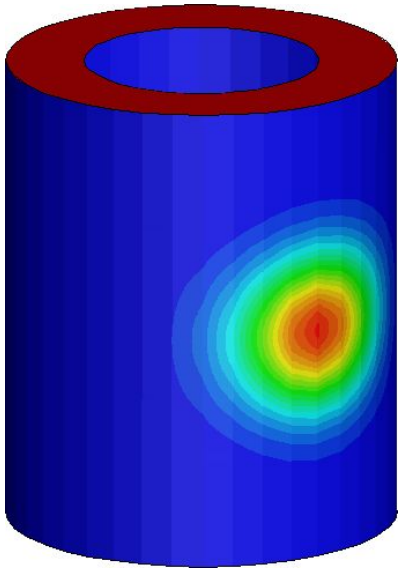

FIG. 2. Thermal boundary condition on the external wall. The max/min temperature of the spot is located at mid-height. The wall thickness is not taken into account in the model. The liquid bridge inside this tube is not shown.

4) The most of the external tube is thermally insulated, and no-slip conditions are imposed for velocity, at $r = R_{out}$:

$$\partial_n T = 0, \quad \vec{V}^g = 0 \quad \text{when} \quad 0 \le z \le L. \tag{10}$$

In order to study the influence of an inhomogeneous thermal environment, on the outer wall a temperature perturbation is introduced in the region centered at the point with coordinates: ($x = R_{out}$, $y = 0$, $z = z_c$), where z_c=6.0 mm. Then temperature boundary conditions will be written in the form:

$$\partial_n T = \frac{1}{k^g} H_f \cdot exp(-\frac{a^2}{A^2}), \tag{11}$$

where value H_f is measured in W/m^2 and defines intensity of external heat impact; this is a parameter of the problem, the constant $A = \sqrt{2.5\cdot10^{-5}}$ m is responsible for the width of a thermal spot, the variable $a = \sqrt{(z-z_c)^2+y^2}$ is measured in m. An example of the boundary condition for positive H_f is shown in Fig. 2.

Calculation of integrated power of this type of external temperature impact on the external wall gives linear dependency

of value H_f with coefficient k_e = 0.01325. So, for example, in case of H_f = 200 W/m^2 it gives external heat impact which is equal to 2.65 mW.

5) The bottom and top sides of the external tube are thermally insulated and zero velocity is imposed.

$$\partial_z T^g = 0, \quad \vec{V}^g = 0 \quad \text{when} \quad z = 0, \quad R_0 < r < R_{out} \quad (12)$$

$$\partial_z T^g = 0, \quad \vec{V}^g = 0 \quad \text{when} \quad z = L, \quad R_0 < r < R_{out} \quad (13)$$

As an initial condition, zero velocity field and mean temperature have been chosen to calculate a steady state. The steady state computed on the same mesh without adding noise was used as initial conditions for time-dependent simulations.

D. Numerical method

Governing equations (1)-(3) with boundary conditions (5)-(13) are solved in dimensional variables using the commercial software ANSYS Fluent 17.2. The solution was obtained for each phase separately, taking into account the boundary conditions at the interface. In order to satisfy the conditions at the interface very accurately, an iterative procedure developed earlier and implemented by means of a user-defined function was used[34].

Computations in multi-domains require a complicated computational mesh, which was generated by the commercial code GAMBIT. A non-uniform grid was chosen for a space discretization as follows. In the azimuthal direction, N_φ = 40 for all the mesh parts. In the liquid domain, $N_z = 60$ with stretch factor 0.973 near the cold and hot corners. In the radial direction, $N_r = 40$, the denser mesh was near the interface with stretch factor 0.97, and a sparse mesh was near the axis with stretch factor 1.03. In the gas domain, the mesh is divided into five parts: an interfacial part, two parts of the length h adjacent to the hot and cold disks and two parts of the length h_{in} adjacent to the rods. The cells number for the interfacial part of the gas phase is the same as for the liquid phase. The problem was solved using dimensional variables (x, y, z), and the variables were transformed accordingly. Numerical convergence was previously tested[33,34,37] for a similar configuration, and we take these results as a reference for validation of the code.

III. RESULTS

The flow in liquid is induced by thermocapillary stresses due to the temperature gradient along the interface. In the steady state, liquid moves from the hot to the cold side along the interface, and the flow pattern consists of one vortex with a center shifted to the hot side. The flow in the gas is driven by the liquid shear. Above the critical value, $\Delta T_{cr} \sim$7 K, the topology of the flow and temperature fields changes, because an oscillatory instability emerges.

To reveal the non-linear dynamics of flow patterns in a liquid bridge under local thermal action on the outer wall, numerical results are presented for two temperature differences between the rods: ΔT = 8.6 and 10 K for various values of H_f. These values of ΔT above the threshold are chosen at different distances from the critical point in order to analyse nonlinear dynamics of the system under local heat impact in the oscillatory state and disclose various modes of instability.

A. Pattern selection near the threshold of instability for ΔT = 8.6 K.

We start investigation of the system dynamics by considering the case with ΔT = 8.6 K which is slightly above the critical value ΔT_{cr}. We expect oscillatory periodic behaviour for all the considered values of H_f.

First, we investigate the reference case, when the system does not include thermal impact on the external wall, i.e., the tube is thermally insulated. The results of non-linear simulations for this case are shown in panels (a), (d), (g) in Fig. 3. The flow structure of the two-phase system is illustrated by the snapshots of the temperature field. The 3-D isosurface of the mean temperature in the liquid (T = 298 K) is embedded in the general temperature field, see panel (a). Around it, the temperature level lines present distribution of the temperature in plane xz for the gas and liquid phases. This image provides overall information about the two-phase temperature distribution, but does not specify the non-linear dynamics. The set of six green snapshots in the top view in panel (d) presents time behavior of the hydrothermal wave over an oscillation period. Two petals of the temperature pattern take on opposite phases after half a period, and then return to their original form, which illustrates the features of a standing wave with a dominant azimuthal wave number m=2. These snapshots define the dominant wave, however, rather often instability exists in the form of mixed modes, which needs further study.

The post-processing approach which has been described previously[33,37] is applied here to precisely define the properties of hydrothermal waves in a three-dimensional flow. In the supercritical region, the time-periodic solution has the form

$$\tilde{F} = \sum_{m=-\infty}^{\infty} \sum_{n=-\infty}^{\infty} \widehat{f}_{m,n}(r,z) \exp(im\phi + in\omega t), \quad (14)$$

where $\widehat{f}_{-m,-n} = \widehat{f^*}_{m,n}$, and n is the number of the combinational Fourier harmonic for the component with wave number m. To examine the properties of a hydrothermal wave F_m with a given azimuthal number m, Eq. (14) is written in the more compact form

$$\tilde{F} = \sum_{m=-\infty}^{\infty} \tilde{f}_m(r,z,t) exp(im\phi). \quad (15)$$

In this study, the non-axisymmetric part of the solution, $\tilde{f}$, is defined by subtracting the steady-state solution F_{steady} obtained on the same mesh:

$$\tilde{f}(r,\phi,z,t) = \tilde{F}(r,\phi,z,t) - F_{steady} \quad (16)$$

For a chosen value of $z = \bar{z}$, we define

$$F_m(t) = \int_0^{R_0} \int_0^{2\pi} \tilde{f}(r,\phi,\bar{z},t) e^{-im\phi} r\,dr\,d\phi = \int \tilde{f}(r,\phi,\bar{z},t) cos(m\phi) r\,dr\,d\phi - i \int \tilde{f}(r,\phi,\bar{z},t) sin(m\phi) r\,dr\,d\phi = Re[F_m(t)] - i\,Im[F_m(t)] \quad (17)$$

where $\tilde{f}$ can be any of $(\mathbf{V}, P, T)$; we select $\tilde{f}$ to be associated with the temperature of the liquid. Thus, $Re(F_m)$ and $Im(F_m)$ are the real and imaginary parts of the oscillatory contribution in 3D flow[37,42].

The map of phase trajectories in Fig. 3(g) supports the previous observation about the dominant standing wave with mode m=2. In addition, the presence of an axially running wave with m=0 can be seen as a line along the negative axis of $Re(F_m)$. The predominance of the hydrothermal wave $m = 2$ with presence of a much weaker mode m=0 explains the perfect symmetry of the patterns in the top view.

Next we examine the case when the external heating with the intensity corresponding to H_f = 200 is imposed on the lateral wall. The results for this case are given in panels (b), (e) and (h) of Fig. 3. The position and intensity of the hot spot are visible on the right side wall in the general view of the temperature field in panel (b). The hottest temperature of the spot is not fixed in the boundary condition, see Eq. (11), and all 3D isosurfaces correspond to T=298 K in this figure for interconnection. Since the number of temperature levels is the same in all three cases, and the level lines are chosen between the maximum and minimum values, the isosurfaces have different colors.

As expected, the 3-D isosurface exhibits a look different from the reference case, for example, its right lateral profile exhibits the predetermined direction towards the hot spot. The temporal behavior in three-dimensional space is very different from the reference case and can be seen in Fig.3b (multimedia view) for H_f=200. The main characteristics of the hydrothermal wave can be revealed by tracing the six top view images in panel (e). The sequence of snapshots clearly demonstrates that the pattern is rebuilding towards the hot spot. This means that external thermal perturbation is responsible for the flow topology. The patterns indicates the presence of a wave with the azimuthal mode m=1, which is influenced by other modes. The phase trajectories in panel (h) detail all available modes: actually, an axially running wave m=0 dominates, then a standing wave with m=1 with presence of m=2 and m=3 modes. Indeed, mentioned above movie presents the main motion from bottom up, but with a tilt towards the hot spot, which changes over time. Also the 4th and 5th snapshots in panel (e) exhibit the features of symmetry typical for m=0.

Another pattern selection occurs in the case of a cooling perturbation on the outer wall. The results for this case are presented in panels (c), (f) and (i) in Fig. 3 for the cooling intensity H_f = -200. The location of the cold spot is visible in the general view of the temperature field. The right profile of the 3D isosurface is repelling from the cold region. The time evolution of the isosurface reveals some features of a standing wave with m=2. The sequence of the snapshots in the top view in Fig 3f (multimedia view) illustrates a strong impact of cooling on the temperature pattern. The typical pattern of a standing wave with m=2 has a dumbbell shape, which reverses its slope every half period, as shown by the 1st and 4th snapshots in panel (d). In the case of a cooled perturbation, there is a time moment when the pattern has a dumbbell shape, see the 2nd shot in panel (f). The pattern then deforms, trying to bounce off the cold side (shots 3 and 4) and finally elongates in such a way as to have less contact towards the cooling disturbance (shots 5 and 6). Analysis of the flow dynamics with phase trajectories in Fig. 3(i) demonstrates that a standing wave m=2 dominates with a considerable presence of m=3. Other modes, such as m=0 and m=1, are only marginal.

Comparison of patterns and phase trajectories for various thermal perturbations makes it possible to highlight several observations. A standing wave with mode m=2 dominates strongly in the reference case (H_f=0), and this is the usual behavior just above the threshold. The flow with mixed modes or a traveling wave emerges further from the critical point. Evidently, thermal perturbations trigger other modes even near the critical point, and it seems that the effect of heating appears to be stronger than that of cooling. At H_f=-200 the dominant mode remains the same as in the reference case, m=2, although with a strong presence of m=3, while at H_f=200 the dominant mode is m=0 and essential contribution of m=1.

A spectral analysis of the liquid bridge flow under various thermal perturbations is presented in Fig. 4. The figure includes a larger range of H_f than that explored in Fig. 3. The dominant oscillation frequency and its two first harmonics for all the cases are gathered in Fig. 4(a). The selected Fourier spectra for H_f=-200 and H_f=200 are shown in panels (b) and (c), respectively. In the reference case, only the dominant frequency f=1.52 Hz is important, while all harmonics are negligible. On a cursory inspection, the lower frequencies for negative H_f appear to be smaller than for H_f=0 despite the assumed identical wavenumber m=2.

The Fourier spectrum in panel (b) for H_f=-200 clarifies this discrepancy. The most powerful frequency is the second one, f_2=1.68 Hz, which has approximately the same value as H_f=0 and presumably corresponds to m=2. The dynamics of f_2 in the negative H_f region indicates that it tends to the frequency of the reference case when $H_f \to 0$. There is no visible correlation between the reference frequency and frequencies in the positive region of H_f in panel (a). The Fourier spectrum at H_f=200 in panel (c) provides f_1=1.00 Hz and f_2=2.00 Hz with approximately equal power. Recall that underlying modes are different from other cases, i.e., m=0 and m=1, which also emphasizes that each mode can have a certain frequency. Furthermore, there is no smooth transition to reference case when $H_f \to 0$ from the right. Again, this spectral analysis demonstrates the important influence of occasional thermal perturbations on the occurrence of oscillatory states.

Originally, the remote thermal perturbations influence the steady state. The presence of perturbations affects the Marangoni force, which is maximal near hot and cold supports, where the temperature gradients are greatest. The thermal impact occurs through the heat transfer by conduction and by convection in gas phase. Thermal conduction from the hot spot located in the middle of the interface reduces temperature

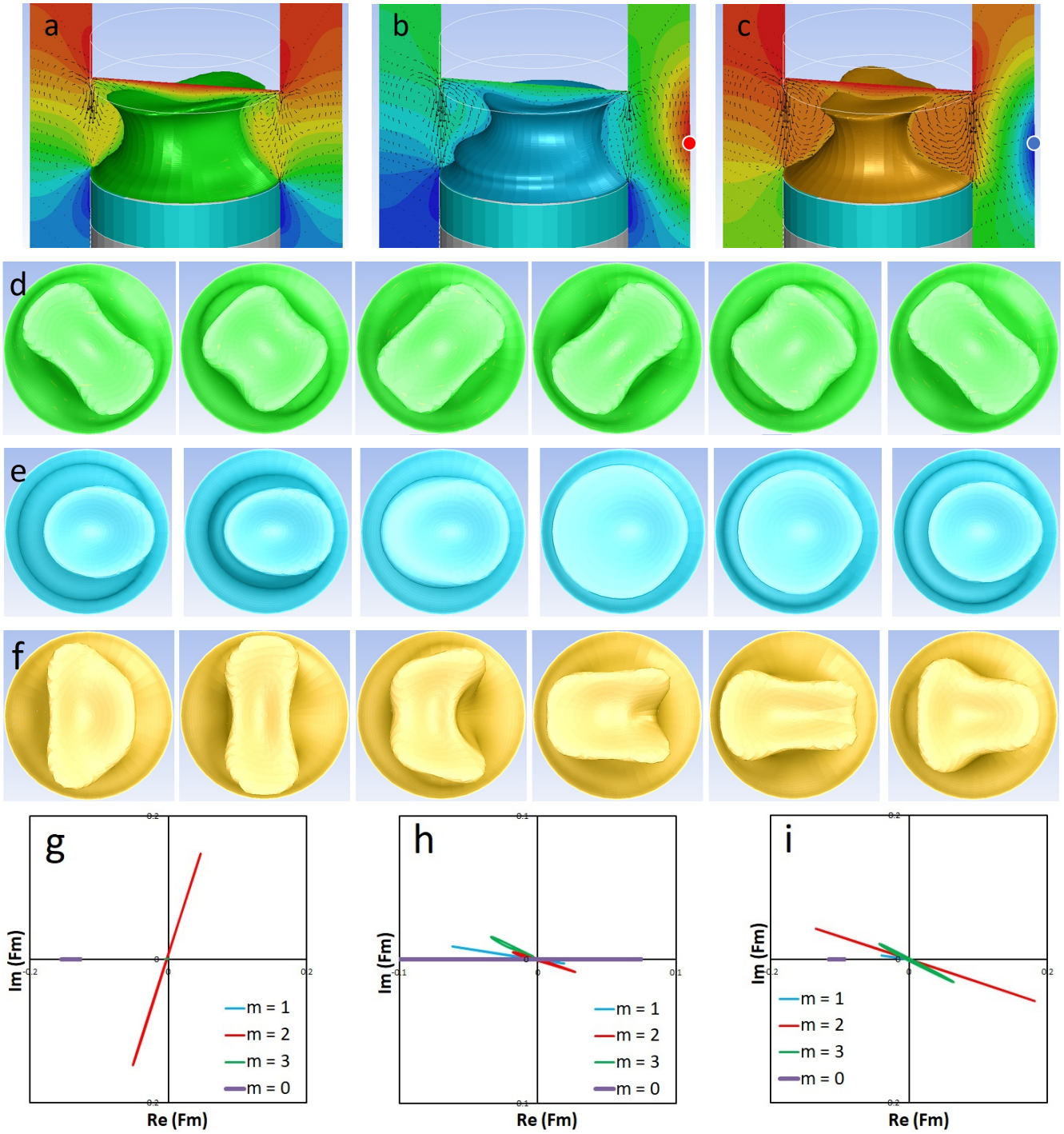

FIG. 3. Results for ΔT = 8.6 K for different temperature impact on the external wall.The upper raw illustrates general temperature field with embedded 3D isosurface T=298 K. The physical meaning of this isosurface is as follows: below this isosurface the liquid is colder than T=298 K, and above is hotter. The position of the hot/cold external perturbation is shown by the red/blue circle. The structure of the flow field is illustrated by arrows. The sequence of the six snapshots in a row presents the top view of the 3D temperature field. The panels (a,d,g) correspond to thermally insulated wall H_f =0 while (b,i,h) correspond to heating with H_f = 200 and 3D isosurface in panel (b) is given in **multimedia view**; panels (c,f,i) corresponds to cooling with H_f = -200 and the top view of panel (f) is given in **multimedia view**.

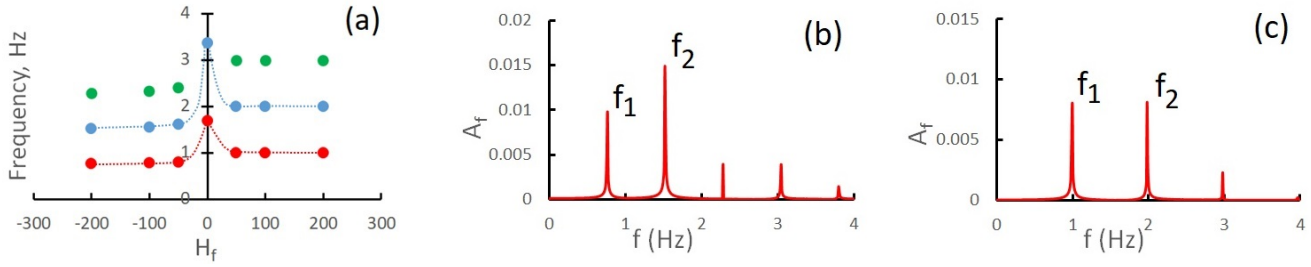

FIG. 4. Spectral analysis of the flow at different thermal perturbations on the external wall near the threshold of instability, ΔT = 8.6 K. (a) Comparison of dominant oscillation frequency and its harmonics at different H_f; the colors correspond to: red - the main frequency, blue - the first harmonic, green - the second harmonic. Fourier spectrum for the (b) H_f = -200 and (c) H_f = 200.

gradient at the upper part and, hence, the interface velocity, which otherwise highest there. Consequently, it will slightly increase the interface velocity at the bottom part. It can be seen in Fig.3b that the lengths of the velocity vectors on the right side of the interface are smaller than those on the left. Situation is reversed in the case of the cold perturbations. The interface velocity rises due to a larger temperature gradient. This is well illustrated by the velocity vectors along the interface in Fig. 3c. We hypothesize that the critical temperature difference can increase in the case of hot perturbations and decrease in the case of cold perturbations, since the motion in liquid is responsible for the instability. However, a deeper analysis of the instability threshold is beyond the scope of this article.

The heat transfer by convection is associated with the role of gravity. The velocity vectors on 3D images in Fig.3 illustrate the role of gravity. In the reference case, the flow in gas is caused only by the liquid shear, and one vortex flow in the gas is directed upward near the outer wall. In the case of hot perturbation (b), shear and buoyancy act in the same direction. Consequently, the gas flow near the wall is stronger than in the reference case. This gas flow entails the hot region upward. In the case of a cold disturbance (c), the shear and buoyancy act in opposite direction, the gas velocity near outer wall decreases sharply. Since buoyancy is more efficient, the cold gas area moves downward.

B. Pattern selection at ΔT = 10 K.

At some distance above the critical point, the flow usually develops as a combination of several modes and the pattern becomes more complex. Here we consider the characteristics of the oscillatory regime at ΔT = 10 K. As in the previous section for smaller ΔT, we start exploring the reference case H_f=0. The results are summarized in panels (a), (d) and (g) in Fig. 5. The global view of the temperature field in panel (a) illustrates the perfect symmetry of the temperature in gas phase from both sides of liquid. The shape of the 3D isosurface is slightly helical, which is a remarkable feature of the classical traveling wave. The sequence of six shots in panel (d) reveals its topology. A pattern with two not very pronounced petals rotates around the center, forming a m=2 traveling wave. As a rule, the phase trajectory of a traveling wave is a circle, but in the considered case it has the shape of a donut. When two modes m=2 and m=0 are present, a bimodal oscillatory flow leads to a 3D torus with a superposition of two motions. A fast cyclic motion is performed around the center along a large-size ellipse. The axis of this ellipse slowly rotates with a low frequency. The visible trajectory in the form of donuts is the projection of a torus onto the plane. It is important to note that the low frequency arises as a result of the nonlinear interaction of waves m=0 and m=2. This particular case has been previously described in detail[33].

The composition of Fig. 5 is different from that of Fig. 3. Along with the reference case, two cases of perturbations by heating of different intensity are examined. The effect of cooling will be discussed separately. Let us first consider the smaller heating, H_f = 100, for which the results are shown in panels (b), (e), and (h). The 3D isosurface reveals a weak helical feature indicative of a traveling wave, although the action of the hot spot breaks the symmetry in xz plane. The sequence of snapshots in panel (e) confirms that oscillatory state is a traveling wave, presumably with presence of the m=1 mode. The phase trajectories shown in Fig. 5(h) represent a rather intricate picture with three traveling waves and m=0. Obviously, among the traveling waves, the m=1 mode dominates which is coherent with the dynamics of the snapshots in panel (e). The contribution of the remaining modes m=0, 2 and 3 is approximately equivalent and much weaker than that of m=1.

It is clear that the oscillations depend on the interaction between the sensitivity of the thermocapillary surface and the intensity of the hot/cold spot. Panels (c), (f) and (i) in Fig. 5 illustrate the results for the external localized heating at H_f = 200. Unexpectedly, the increase of the external heating leads to simplification of the system dynamics. The 3D isosurface in panel (c) at ΔT=10 K looks similar as at a smaller temperature difference ΔT = 8.6 K in Fig. 3(b). The sequence of snapshots in panel (f) is also quite similar to that one in Fig. 3(e). The phase trajectories in panel (i) also underline the similarity with Fig. 3(h). The non-linear dynamics is governed by the dominant m=0 mode, which is an axially running wave, with visible presence of m=1 and smaller contribution of m=2 and 3. The spectral analysis in Fig. 6(a) illustrates one dominant frequency, and its value, f=1.07 Hz, is slightly higher (by 7%) than at ΔT = 8.6 K

Next we consider the effect of perturbations by cooling at ΔT = 10 K. The results for different cooling intensities, H_f

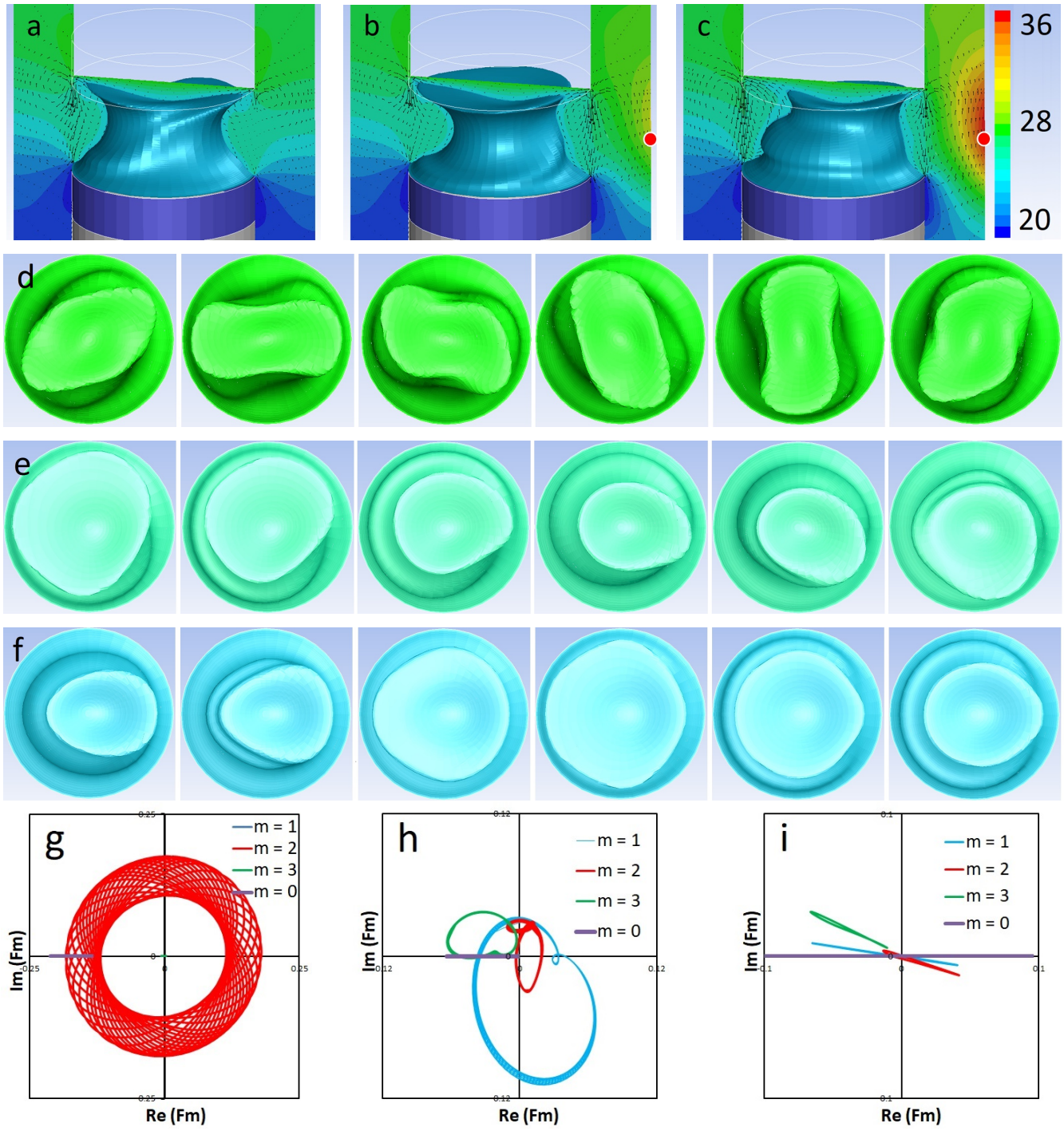

FIG. 5. Topology of the temperature field at ΔT = 10.0 K under different thermal action on the lateral wall: panels (a,d,g) correspond to thermally insulated wall H_f =0; (b,i,h) to low heating H_f = 100, (c,f,i) to higher heating H_f = 200. The upper row illustrates overall temperature field with embedded 3D isosurface corresponding to T=298 K. The sequence of the six snapshots in a row presents the top view of the 3D temperature field. The low row shows the phase trajectories.

= -100 and H_f = -200, are summarised in Fig. 7. Both 3D isosurfaces for T=298 K, shown in panels (a) and (b), look somewhat similar and sophisticated. The helical feature of the three-dimensional figures indicates a traveling wave. The snapshots in panels (c) and (d) reveal rotation of the 3D patterns for both H_f. However, despite the similar boundary conditions, the hydrothermal wave at H_f=-100 travels in counterclockwise direction, see in Fig.7c (multimedia view), while a wave at H_f=-200 travels in clockwise direction, see Fig.7d (multimedia view). The change in the wave traveling direction

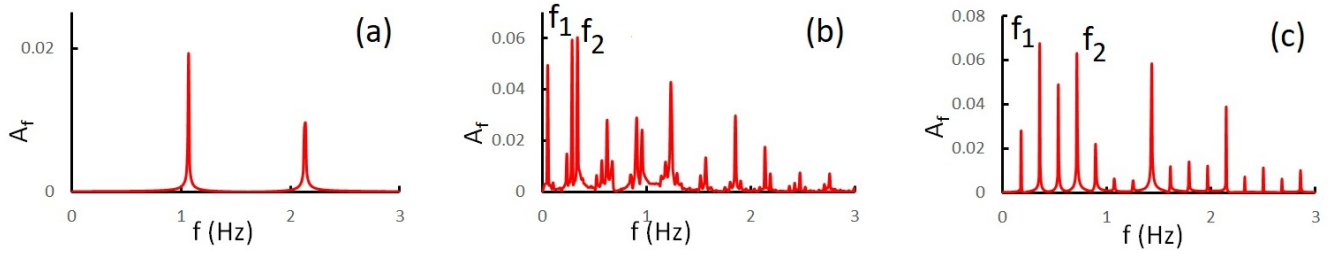

FIG. 6. Spectral analysis of the flow at different thermal perturbations on the external wall near the threshold of instability, ΔT = 10 K. (a) Fourier spectrum for the (a) H_f = 200 , (b) H_f = -100 and (c) H_f = -200.

is enigmatic: in the reference case ($H_f = 0$), the hydrothermal wave rotates clockwise, when the outer wall cools down to a level corresponding to H_f = -100, it changes direction; however, at deeper cooling, H_f = -200, the hydrothermal wave rotates clockwise again. Despite the different directions of traveling waves, the phase trajectories at H_f = 0 and H_f = -100 illustrate the donut topology associated with quasi-periodic motion forming a torus in three-dimensional phase space. As discussed above, the torus is the result of bimodal oscillations formed by the m=0 and m=2 modes. Indeed, the Fourier spectrum at H_f=-100 in Fig. 6(b) displays two very close frequencies f_1 and f_2 associated with the m=0 and m=2 modes, and a very low frequency (f=0.051 Hz). Again, the low frequency responsible for the torus formation arises as a result of the nonlinear interaction of waves m=0 and m=2.

Another interesting aspect is observed in Fig. 7(f) for H_f = –200. It illustrates that the phase trajectories of the m=2 mode are not closed. This suggests that the center of the cycle is continuously shifted. An explanation follows from the presence of the mode m=0 which shifts the center of the phase plane and provides filling between the two cycles. Unlike the case H_f = –100, the frequencies f_1 and f_2 in Fig. 6(c) are not so close to form the low frequency which would be responsible for the torus formation, compare the spectral behavior of panels (b) and (c) in Fig. 6.

The analysis above with more complicated patterns and phase trajectories at ΔT=10 K emphasizes that the temperature perturbations of the outer wall by the cooling in the system at a certain distance above the critical point is much stronger than in its vicinity.

C. Overview of the hydrothermal stability under action of thermal disturbances on the outer wall

Figure 8 summarizes, in terms of intensity of thermal disturbances H_f and applied thermal stress ΔT, different ways that a liquid bridge responds to the thermal perturbations on the outer wall. At ΔT=8.6 K ($\sim$ 15% above critical point), this diagram of hydrothermal wave properties immediately reveals (panel a) that standing waves (blue symbols) are the most common modes of instability. For cooling perturbations ($H_f < 0$), as well as in the thermally isolated case, the instability develops with the azimuthal wave number m=2. When the surrounding tube is subjected to thermal perturbation by heating, a mode transition occurs and the standing wave changes its symmetry to m=1. Summing up, this suggests that hydrothermal instability near the threshold emerges in the form of a standing wave, but the critical wavenumber depends on the thermal perturbation.

At ΔT=10 K ($\sim$ 45% above critical point), a traveling wave with m=2 dominates in the region with thermal perturbations $-200 < H_f < 50$. In addition, the phase trajectories form a kind of donut, but they are winding around a circle, not closed. This suggests that the trajectories are projections of a multi-dimensional torus on a plane[33]. At higher positive H_f, the instability manifests itself as an alternation of traveling and standing waves with the dominant m=1 mode but with a strong presence of other modes.

The explanation of the appearance and disappearance of a quasi-periodic torus topology can be explained by the spectral analysis of temperature fluctuations in a liquid bridge. In all the cases where torus is formed, the m=2 mode co-exists with the m=0 mode leading to Fourier spectrum with multiple frequencies, see Fig. 6(b,c). If the interaction of these modes leads to a very low frequency (panel b), then a torus with closed trajectories forms, if the resulting frequency is higher, then the trajectories are winding.

Let us briefly discuss the change in the heat flux across the interface. The local heat flux through the unit of the free surface area at $r = R_0$ is defined as

$$q = -k_l \partial_r T \tag{18}$$

The negative sign shows that the heat flux moves from higher temperature regions to lower temperature regions. The net flux through the unit of the free surface can be defined as $\overline{q} = \int q(z)dz$.

Fig. 8(b) shows a dependence of a net heat flux $\overline{q}$ through the liquid-gas interface on heat impact on the external wall for various temperature differences ΔT between rods. In absence of any impact (H_f = 0) the liquid bridge is warmer than the ambient gas and it emits the heat. It is obvious that this heat emission is growing with temperature difference increase. In presence of local heating of the external wall, the ambient gas becomes warmer, so the heat flux through the interface is linearly decreasing when the value of H_f becomes larger. In the opposite case, when the system is subjected to a local cooling, the heat flux is growing for the negative values of H_f.

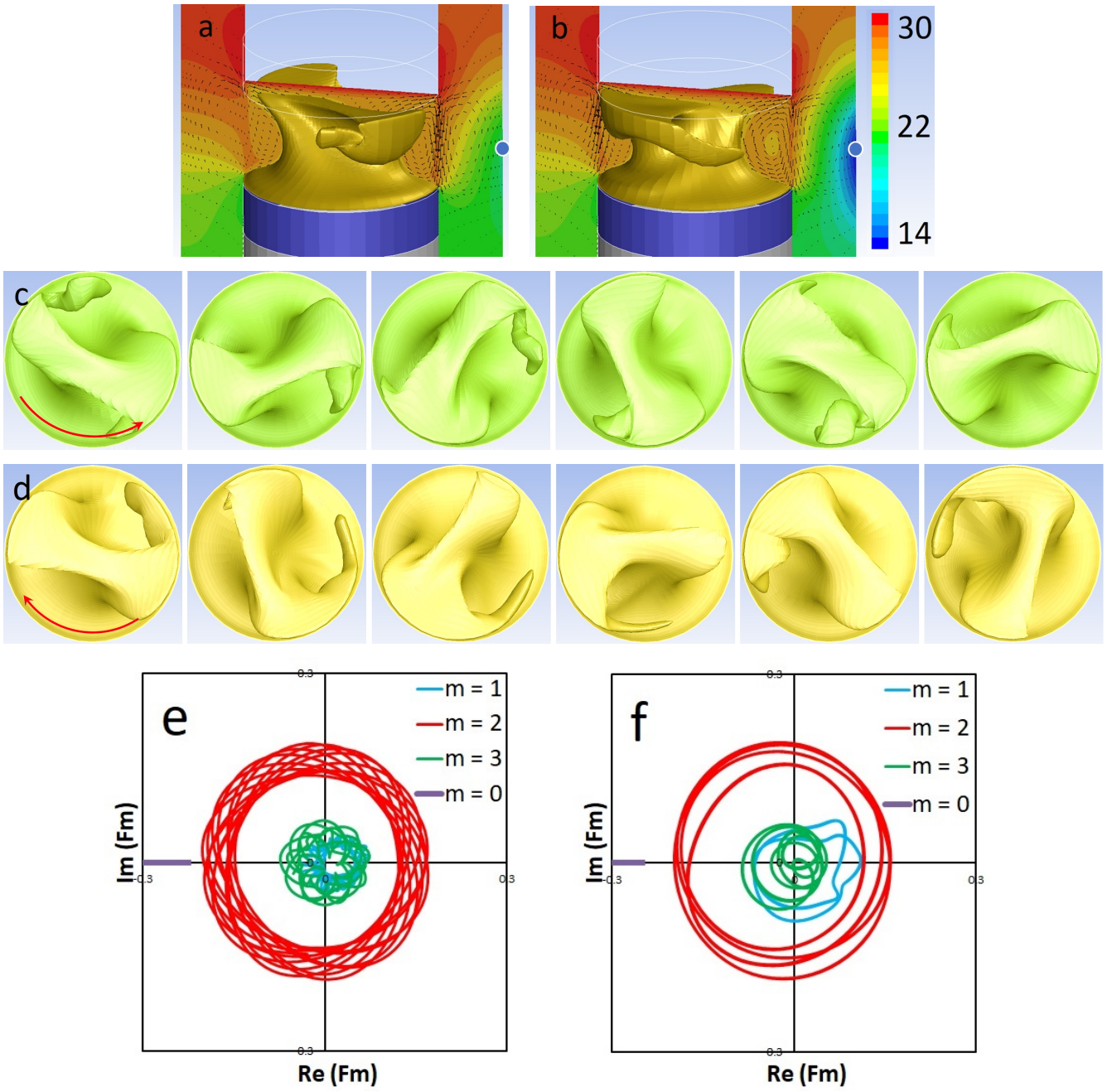

FIG. 7. Topology of the temperature field at ΔT = 10.0 K under thermal action on the lateral wall by the cooling effect of different intensities (a), (c) H_f = -100, (b),(d) H_f = -200. At H_f = -100, panel (c) (**multimedia view**), the wave travels counter-clockwise, while at H_f = -200 panel (d) (**multimedia view**), the wave travels clockwise. The phase trajectories are given at the bottom row, (e) H_f = -100, (f) H_f = -200.

IV. CONCLUSIONS

In this work, the effect of a remote heat/cold source on the instability dynamics of a liquid bridge surrounded by a gas is numerically studied. The hydrothermal wave instability was explored for two temperature differences ΔT by varying the intensity of thermal perturbations over a wide range. As a main result, thermal perturbations of the remote wall have a strong influence on the nonlinear dynamics of the flow, even though the gas with low heat conductivity is located between the liquid bridge interface and the outer wall.

Not far from the critical point, at ΔT = 8.6 K ($\sim$ 15% higher), a striking difference was observed between the effect of warm and cold configurations. In the reference case H_f=0, corresponding to a thermally insulated system, the instability manifests itself as a standing wave with m=2. At the locally cooled external wall, $H_f < 0$, the dominant mode remains the same as in the reference case, m=2, but the temperature pattern

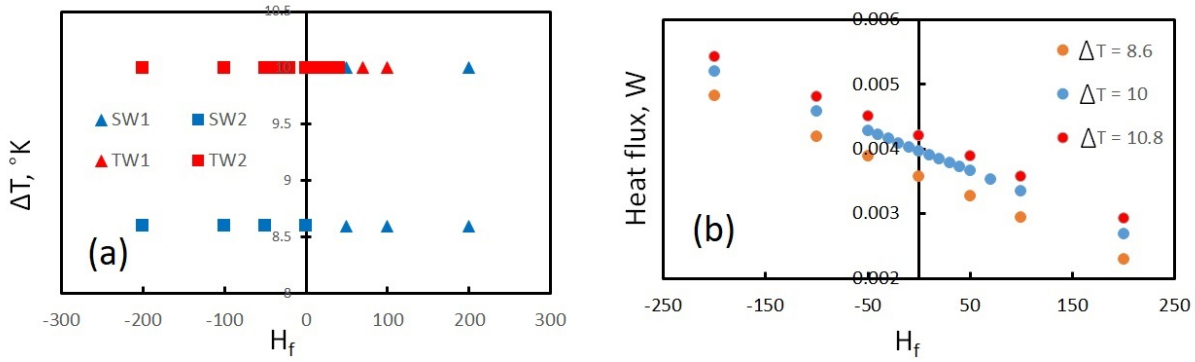

FIG. 8. Overview of the hydrothermal instability observed in a liquid bridge under the influence of external thermal perturbations. (a) Properties of hydrothermal waves; (b) the net heat flux $\bar{q}$ through the interface of the liquid bridge.

is greatly different. Thermal perturbations trigger secondary standing waves with different modes, which complicates the flow pattern.

Further to supercritical region, $\Delta T = 10\dot{\mathrm{K}}$ ($\sim 45\%$ higher), the non-linear dynamics becomes more complex. A traveling wave with m=2 dominates in the region with thermal perturbations $-200 < H_f < 50$. The first remarkable feature of the instability in this region is that the traveling wave changes the direction of rotation depending on H_F. In the reference case (H_f = 0), the hydrothermal wave rotates clockwise, at H_f = -100 it changes direction to counterclockwise, and at deeper cooling, H_f = -200, the hydrothermal wave rotates clockwise again. is an observation and we do not insist that the H_f value is responsible for this. We recall that no perturbations are introduced into the numerical scheme, and all non-steady simulations start with a 2D steady state obtained on the same mesh. The oscillatory solution in all the cases includes several azimuthal modes, and the phase trajectories show that they do not rotate in the same direction. In particular, for H_f=0 and H_f=-200 the trajectories of all modes are wound clockwise with time, and for H_f=-100 the m=2,3 modes are wound counter clockwise while m=1 clockwise. The global rotation of the three-dimensional pattern depends on the direction of the dominant mode, while its topology depends on the mutual direction of the various modes.

Another remarkable feature is that the phase trajectories form a kind of donut, representing projections of a three-dimensional torus in the phase space. The torus originates from two hydrothermal waves with distinct (close) frequencies. In the case of hot perturbations, $H_f > 0$, the change in oscillatory state occurs more distinctly. The preferred modes are m=0 (axially traveling wave) and m=1 (a standing wave), and their dominance alternates with a change in H_f.

The developed analysis allowed us to explore in detail the effect of thermal disturbances at distant walls on the nonlinear flow dynamics, thus providing valuable information how important to control the surrounding conditions. The presence of external local sources should be carefully taken into account in the experimental setup and industry.

ACKNOWLEDGMENTS

The work of Y.G. was supported by the PRODEX programme of the Belgian Federal Science Policy Office. The work of V.S. was supported by MMASINT (KK-2022/00047) and IT1505-22 (Research Group Program) of the Basque Government.

CONFLICT OF INTEREST

The authors have no conflicts to disclose.

DATA AVAILABILITY STATEMENT

The data that supports the findings of this study are available within the article.

REFERENCES

[1]D. Schwabe, "Marangoni effect in crystal growth melts," PCH. Physicochemical hydrodynamics **2**, 263–280 (1981).
[2]A. Cröll, W. Müller-Sebert, K. W. Benz, and R. Nitsche, "Natural and thermocapillary convection in partially confined silicon melt zones," Microgravity Sci. Technol. **3**, 204–215 (1991).
[3]K. C. Mills, B. J. Keene, R. F. Brooks, and A. Shirali, "Marangoni effects in welding," Philosophical Transactions: Mathematical, Physical and Engineering Sciences **356**, 911–925 (1998).
[4]F. J. Higuera, "Liquid-fuel thermocapillary flow induced by a spreading flame," J. Fluid Mech. **473**, 349–377 (2002).
[5]R. Varas, P. Salgado Sanchez, J. Porter, J. Ezquerro, and V. Lapuerta, "Thermocapillary effects during the melting in microgravity of phase change materials with a liquid bridge geometry," International Journal of Heat and Mass Transfer **178**, 121586 (2021).
[6]B. Seta, D. Dubert, M. Prats, J. Gavalda, J. Massons, M. Bou-Ali, X. Ruiz, and V. Shevtsova, "Transitions between nonlinear regimes in melting and liquid bridges in microgravity," Int. J. Heat Mass Transfer **193**, 122984 (2022).
[7]P. Ehrhard and S. H. Davis, "Non-isothermal spreading of liquid drops on horizontal plates," J. Fluid Mech. **229**, 365–388 (1991).
[8]D. Schwabe, A. Scharmann, F. Preisser, and R. Oeder, "Experiments on surface tension driven flow in floating zone melting," Journal of Crystal Growth **43**, 305–312 (1978).

[9]H. C. Kuhlmann, Thermocapillary Convection in Models of Crystal Growth, Vol. 152 (Springer-Verlag, Berlin, 1999).
[10]M. Lappa, Thermal Convection: Patterns, Evolution and Stability (John Wiley & Sons, 2009).
[11]D. Schwabe, "Thermocapillary liquid bridges and Marangoni convection under microgravity. results and lessons learned." Microgravity Sci. Technol. **26**, 1–10 (2014).
[12]C. Le, L. Liu, and Z. Li, "Oscillatory thermocapillary convection in deformed half zone liquid bridges of low Prandtl number fluids," Intl. Communications Heat Mass Transfer **127**, 105499 (2021).
[13]M. Wanschura, V. M. Shevtsova, H. C. Kuhlmann, and H. J. Rath, "Convective instability mechanisms in thermocapillary liquid bridges," Phys. Fluids **7**, 912–925 (1995).
[14]V. M. Shevtsova and J. C. Legros, "Oscillatory convective motion in deformed liquid bridges," Phys. Fluids **10**, 1621–1634 (1998).
[15]Q.-S. Chen, W.-R. Hu, and V. Prasad, "Effect of liquid bridge volume on the instability in small-prandtl-number half zones," J. Crystal Growth **203**, 261–268 (1999).
[16]J. Leypoldt, H. C. Kuhlmann, and H. J. Rath, "Three-dimensional numerical simulation of thermocapillary flows in cylindrical liquid bridges," J. Fluid Mech. **414**, 285–314 (2000).
[17]M. Lappa, R. Savino, and R. Monti, "Three-dimensional numerical simulation of marangoni instabilities in non-cylindrical liquid bridges in microgravity," Int. J. Heat Mass Transfer **44**, 1983–2003 (2001).
[18]C. Nienhüser and H. Kuhlmann, "Stability of thermocapillary flows in noncylindrical liquid bridges," J.Fluid Mech. **458**, 35–73 (2002).
[19]D. E. Melnikov, V. M. Shevtsova, and J. C. Legros, "Onset of temporal aperiodicity in high prandtl number liquid bridge under terrestrial conditions," Physics of Fluids **16**, 1746–1757 (2004).
[20]Y. Kamotani, L. Wang, S. Hatta, A. Wang, and S. Yoda, "Free surface heat loss effect on oscillatory thermocapillary flow in liquid bridges of high prandtl number fluids," International Journal of Heat and Mass Transfer **46**, 3211–3220 (2003).
[21]A. Wang, Y. Kamotani, and S. Yoda, "Oscillatory thermocapillary flow in liquid bridges of high prandtl number fluid with free surface heat gain," International Journal of Heat and Mass Transfer **50**, 4195–4205 (2007).
[22]M. Irikura, Y. Arakawa, I. Ueno, and H. Kawamura, "Effect of ambient fluid flow upon onset of oscillatory thermocapillary convection in half-zone liquid bridge," Microgravity-Science and Technology **16**, 176–180 (2005).
[23]T. Watanabe, D. E. Melnikov, T. Matsugase, V. Shevtsova, and I. Ueno, "The stability of a thermocapillary-buoyant flow in a liquid bridge with heat transfer through the interface," Microgravity-Science and Technology **26**, 17–28 (2014).
[24]T. Yano, K. Nishino, I. Ueno, S. Matsumoto, and Y. Kamotani, "Sensitivity of hydrothermal wave instability of marangoni convection to the interfacial heat transfer in long liquid bridges of high prandtl number fluids," Physics of Fluids **29**, 044105 (2017).
[25]T. Yano, M. Hirotani, and K. Nishino, "Effect of interfacial heat transfer on basic flow and instability in a high-prandtl-number thermocapillary liquid bridge," Int. J. Heat Mass Transfer **125**, 1121–1130 (2018).
[26]T. Yano, K. Nishino, S. Matsumoto, I. Ueno, A. Komiya, Y. Kamotani, and N. Imaishi, "Report on microgravity experiments of dynamic surface deformation effects on marangoni instability in high-prandtl-number liquid bridges." Microgravity Sci. Technol. **30**, 599–610 (2018).
[27]Q. Kang, D. Wu, L. Duan, L. Hu, J. Wang, P. Zhang, and W. Hu, "The effects of geometry and heating rate on thermocapillary convection in the liquid bridge," Journal of Fluid Mechanics **881**, 951–82 (2019).
[28]D. Melnikov and V. Shevtsova, "The effect of ambient temperature on the stability of thermocapillary flow in liquid column," Int. J. Heat Mass Transfer **74**, 185 – 195 (2014).
[29]B. Xun, K. Li, W.-R. Hu, and N. Imaishi, "Effect of interfacial heat exchange on thermocapillary flow in a cylindrical liquid bridge in microgravity," Int. J. Heat Mass Transfer **54**, 1698–1705 (2011).
[30]D. Melnikov, V. Shevtsova, T. Yano, and K. Nishino, "Modeling of the experiments on the Marangoni convection in liquid bridges in weightlessness for a wide range of aspect ratios," Int. J. Heat Mass Transfer **87**, 119 – 127 (2015).
[31]F. Romano and H. C. Kuhlmann, "Heat transfer across the free surface of a thermocapillary liquid bridge." Tech. Mech. **39**, 72–84 (2019).
[32]N. Shitomi, T. Yano, and K. Nishino, "Effect of radiative heat transfer on thermocapillary convection in long liquid bridges of high-Prandtl-number fluids in microgravity," Int. J. Heat Mass Transfer **133**, 405–415 (2019).
[33]Y. Gaponenko, V. Yasnou, A. Mialdun, A. Nepomnyashchy, and V. Shevtsova, "Effect of the supporting disks shape on nonlinear flow dynamics in a liquid bridge," Physics of Fluids **33**, 042111 (2021).
[34]V. Shevtsova, Y. Gaponenko, and A. Nepomnyashchy, "Thermocapillary flow regimes and instability caused by a gas stream along the interface," J. Fluid Mech. **714**, 644–670 (2013).
[35]V. Shevtsova, Y. Gaponenko, H. C. Kuhlmann, M. Lappa, M. Lukasser, S. Matsumoto, A. Mialdun, J. M. Montanero, K. Nishino, and I. Ueno, "The JEREMI-project on thermocapillary convection in liquid bridges. Part B: Overview on impact of co-axial gas flow," Fluid Dyn. Mat. Process **10**, 197–240 (2014).
[36]V. Yasnou, Y. Gaponenko, A. Mialdun, and V. Shevtsova, "Influence of a coaxial gas flow on the evolution of oscillatory states in a liquid bridge," Int. J. Heat Mass Transfer **123**, 747–759 (2018).
[37]Y. Gaponenko, V. Yasnou, A. Mialdun, A. Nepomnyashchy, and V. Shevtsova, "Hydrothermal waves in a liquid bridge subjected to a gas stream along the interface," J. Fluid Mech. **908**, A34 (2021).
[38]R. Liang, X. Jin, S. Yang, J. Shi, and S. Zhang, "Study on flow structure transition in thermocapillary convection under parallel gas flow," Exp. Therm. and Fluid Sci. **113**, 110037 (2020).
[39]Stojanovic and H. M., Kuhlmann, "Stability of thermocapillary flow in high-Prandtl-number liquid bridges exposed to a coaxial gas stream," Microgravity Sci. Technol. **32**, 953–959 (2020).
[40]Y. Gaponenko, A. Mialdun, and V. Shevtsova, "Shear driven two-phase flows in vertical cylindrical duct," Int. J. Multiphase Flow **39**, 205–215 (2012).
[41]J. M. Montanero, G. Cabezas, J. Acero, and J. M. Perales, "Theoretical and experimental analysis of the equilibrium contours of liquid bridges of arbitrary shape," Phys. Fluids **14**, 682–693 (2002).
[42]V. Shevtsova, D. E. Melnikov, and A. Nepomnyashchy, "New flow regimes generated by mode coupling in buoyant-thermocapillary convection," Phys. Rev. Lett. **102**, 134503 (2009).